

# Modeling of local hydrogen concentration on microscopic scale to characterize the influence of stress states and non-metallic inclusions in pipeline steels

Berk Tekkaya <sup>\*</sup>, Michael Dölz, Sebastian Münstermann

*Institute of Metal Forming, RWTH Aachen University, Aachen, Germany*

## ARTICLE INFO

### Keywords:

Hydrogen diffusion  
Crystal plasticity  
Non-metallic inclusions  
RVE  
Stress state

## ABSTRACT

Hydrogen as an energy carrier plays an important role in achieving the ambitious climate targets associated with decarbonization. The main challenge is to ensure safe transport of gaseous respectively liquid hydrogen through the already existing natural gas pipelines. Since experimental methods, such as hydrogen-induced-cracking tests, fail to provide quantitative answers to the question of which local effects/mechanisms trigger failure under hydrogen loading, complex numerical multi-scale approaches are needed. In this work, a phenomenological crystal plasticity model based on dislocation slip mechanisms was implemented in Abaqus/Implicit and coupled with a hydrogen diffusion model to investigate the influence of microstructural characteristics in terms of grain size, texture, phase fraction but also lattice defects such as dislocations, grain boundaries, carbides, and non-metallic inclusions on hydrogen-induced-damage behavior. As a driving force for hydrogen diffusion, both hydrostatic stresses and plastic strains associated with mechanically and thermally induced residual stresses under various stress states were investigated. It was found that the impurity degree of the steel in terms of non-metallic inclusions plays an important role in hydrogen susceptibility in two aspects, namely geometrically (notch-effect) and in the generation of residual stresses. The effect of matrix shrinkage on the inclusions and the resulting stress field after cooling leads to the accumulation of hydrogen atoms around the inclusions, resulting in locally high critical concentrations. The simulations performed on microstructures with and without non-metallic inclusions under different stress states demonstrated the notched effect that the presence of non-metallic inclusions increases the local hydrogen concentration up to 28 %.

## 1. Introduction

Hydrogen as an energy carrier offers the potential to realize a CO<sub>2</sub>-neutral energy supply [1,2]. Hydrogen as a gas can be used in heat and power generation as well as in mobility. The transport of hydrogen through the existing structure of natural gas pipelines is planned and supported by the European Union through the so-called Green Deal [3], RePowerEU [4,5] and Fit for 55 [6] initiatives. Based on these proposals, Wang et al. [7] presented the European Hydrogen Backbone (EHB) strategy which is extended by Jens et al. [8] including 21 additional countries. EHB intends to provide a pipeline network of about 53,000 km by 2040 to transport enough hydrogen across Europe for several applications. Hereby, 60 % of this pipeline network should be based on the existing (old) natural gas pipelines. However, it is well-known that natural gas pipelines have a hydrogen embrittlement issue [9–13]. As an

example, the pipe explosion near Carlsbad, New Mexico in 2000 based on pipeline accident report NTSB/PAR-03/01 can be given [14]. Thus, a safe transport of hydrogen has a major priority. Most of the pipe failures in the past are rooted in so-called hydrogen-induced-cracking (HIC). This phenomenon can be described according to the pressure theory [15, 16], as hydrogen atoms diffusing into the metal lattice and accumulating in lattice defects such as dislocations, grain boundaries as well as non-metallic inclusions, where they can then recombine into hydrogen molecules. Since hydrogen molecules occupy more space than individual hydrogen atoms, this results in an increase in pressure in the metal lattice. Thus, micro cracks can initiate, accumulate and lead to a fatal failure [17,18]. As also mentioned by Findley et al. [9] and Falkenberg et al. [19], the driving force for HIC is not necessarily the applied external loads but inner or residual stresses. The type of fracture either ductile or brittle caused by HIC depends on the activated mechanism. On

\* Corresponding author.

E-mail address: [berk.tekkaya@ibf.rwth-aachen.de](mailto:berk.tekkaya@ibf.rwth-aachen.de) (B. Tekkaya).

the one hand, the plastic strain driven hydrogen-enhanced localized plasticity (HELP) mechanism results in ductile fracture through the increase in dislocation mobility, since hydrogen atoms reduce the barriers of dislocations at crack tip [20–22]. On the other hand, the stress driven hydrogen enhanced decohesion (HEDE) mechanism leads to brittle fracture due to the weakening of interatomic bonding forces by reducing the cohesive energy of the matrix [23–25]. A combined interaction of the mechanisms HELP and HEDE is called adsorption induced dislocation emission (AIDE) [26].

Yazdipour et al. [27] analyzed the role of grain boundaries for hydrogen diffusion in X70 steel. For this purpose, they applied the cellular automata approach and created 2d models. The simulations performed showed that hydrogen atoms diffuse faster in larger grains than in small grains, which was in good agreement with the permeation tests. They also observed that hydrogen atoms diffuse across grain boundaries and accumulate there until a critical hydrogen concentration is reached. After that, diffusion takes place within the grain. Arenas-Salcedo et al. [28] conducted an experimental study to determine the influence of carbon amount and microstructure on hydrogen diffusion in X52, X60, X65 and X70 steels. They concluded that both the hydrogen diffusion coefficient and the maximum oxidation current achieved higher values in the case of a steel with a lower carbon percentage. They also found that these parameters peaked for the bainitic microstructure compared to the ferritic-pearlitic microstructure. Hussein et al. [29] investigated the effect of yield strength, anisotropy, and uniaxial tensile loading on hydrogen concentration using 2d RVE (representative volume element) models for  $\alpha$ -iron and high strength steel. They found that hydrogen atoms cluster in both lattice and trap sites at grain boundaries, while higher strength minimizes the contribution of hydrogen concentration coming from trapping sites. However, they did not consider the influence of non-metallic inclusions in their analyses. In addition, the RVEs were meshed with triangular elements, which do not provide as accurate results as quadratic elements when calculating the gradient of hydrostatic stress as driving force for hydrogen diffusion. This results in a prediction of less hydrogen concentration ( $\approx 24\%$ ) with triangular elements [30]. Ilin et al. [31] studied the influence of microstructural heterogeneities on hydrogen diffusion in 316 L stainless steel under uniaxial loading. Therefore, they built 2d RVE composed of 110 grains, which were meshed by triangular elements. They discovered that the hydrogen concentration in the interstitial sites has the greatest influence, and the maximum concentration occurs at grain boundaries with high hydrostatic stress. Tao et al. [32] examined hydrogen diffusion in ferrite and austenite in the rolling direction and transverse to the rolling direction by the case of a duplex stainless steel. For this purpose, they used 2d RVEs meshed with quadratic elements and implemented hydrogen diffusion model under considering different diffusivity as well as solubility values for corresponding phases. They concluded that hydrogen diffusion mainly takes place in ferrite and stretched austenite grains lead to higher diffusivity. Hassan et al. [33] analyzed the coupled hydrogen diffusion under biaxial loading. Similar to the studies presented above, they also applied 2d RVEs neglecting the influence of substructures and non-metallic inclusions. They found that hydrogen atoms diffuse from compressive to tensile loaded regions. Kumar et al. [34] presented a framework to model fatigue behavior under hydrogen loading of polycrystalline nickel. They extended the kinematics in non-local physics-based CP model with an elastic stretching deformation gradient to consider the effect of hydrogen atoms. For the fatigue modeling based on HELP and HEDE mechanisms, a fatigue indicator parameter was implemented as a function of hydrogen concentration, grain boundary normal stress and equivalent plastic strain. The simulations were performed on 3d RVE with 16 grains. Zhang et al. [35] investigated hydrogen diffusion in pure iron using phase field method, where they focused on grain boundaries as hydrogen traps. The performed simulations were carried out using a 2d model with 23 grains. They concluded that grain boundaries can increase or decrease the hydrogen diffusivity depending on trap

activation energy for face-centered-cubic microstructure. In another study, Mohtadi-Bonab MA et al. [36] modeled HIC caused by inclusions using the J-Integral concept of fracture mechanics in case of API 5L X70. In their model, the inclusions were considered as voids and internal pressure was applied as a boundary condition to get local stress peaks. The micro-crack was introduced in the simulation where the J-Integral has its maximum. With this approach, they were able to predict the crack initiation from inclusions sites and showed that a large crack can form between closely placed inclusions. However, they did not model the hydrogen diffusion and did not consider the influence of the microstructure in terms of RVEs and CP model.

Based on the literature review presented, we conclude there is no 3d microstructure modeling yet that takes into account the substructures, which results from the hierarchical structure of the martensitic or bainitic microstructure, and the degree of impurity regarding non-metallic inclusions when studying the influence of microstructure on hydrogen diffusion. In addition, the influence of the stress state on hydrogen diffusion at the microscale has not been studied in detail in the literature. Moreover, hydrostatic stresses caused by mechanical loading are motivated to be the driving force for hydrogen diffusion in the microstructure, but the effect of thermal loading in terms of a cooling process is not truly investigated yet. The innovation of this work is to fill this gap in the literature and develop a numerical framework in which 3d RVEs with substructures and non-metallic inclusions are generated and loaded under different stress states. In addition, both mechanically and thermally induced residual stress fields are investigated as a driving force for hydrogen diffusion. For the modeling approach, a phenomenological CP model is implemented in Abaqus/Implicit and coupled with the hydrogen diffusion model. It is noteworthy that focusing only on the microstructure is not sufficient to characterize hydrogen diffusion and the corresponding damage behavior, one needs to consider the whole process chain in different scales. To close the gap in the literature the authors aim to make the first step to develop a multi-scale approach to examine hydrogen resistance of pipeline steels starting from the effect of microstructure regarding grain size, texture, phase fraction, substructures and non-metallic inclusions based on 3d RVEs, then considering the damage mechanics behavior on the mesoscale for structural analysis and finally on macroscale the influence of the conventional U-O-E pipe forming process on hydrogen diffusion. This paper truly focuses on the microscale and is hypothesizing that non-metallic inclusions have two major impacts on hydrogen susceptibility of pipeline steels. On the one hand, non-metallic inclusions act as a so-called notched effect and causes stress peaks in the interface between matrix and inclusion under mechanical loading. These local areas serve as excellent hydrogen traps. On the other hand, under thermal loading, such as cooling process after hot rolling, matrix shrinks on non-metallic inclusions and the resulting inhomogeneous deformations lead to residual stresses around the inclusions. Therefore, hydrogen atoms preferentially localize around the inclusions and when the critical hydrogen concentration is reached, HIC initiates starting from the inclusions sites.

## 2. Material characterization

The material API-5L X65 (pipeline steel) was delivered as a plate with the dimensions  $300 \times 400 \times 30 \text{ mm}^3$ . It was thermomechanically rolled and quenched, which resulted in improved weldability in addition to good toughness. Its chemical composition was investigated on plane-ground samples with an optical emission spectrometer by two indents at different places, and the mean values are given in Table 1. The material is a low-carbon Al-killed steel with a relatively high amount of Cu, as Cu

**Table 1**

Chemical composition of X65 in wt.-%.

C	Si	Mn	Cr	Ni	Cu	Al	Nb
<0.03	<0.3	<1.5	<0.2	<0.5	<0.5	<0.3	<0.05

increases the strength of the material, while it reduces the HIC susceptibility [12]. Furthermore, the chemical composition is optimized with respect to the role of microalloying elements, such as Nb.

Light microscopy (LOM) of X65 was performed to analyze the microstructure. Fig. 1a shows the corresponding microstructure after nital etching, from which it can be concluded that the material has a ferritic-bainitic microstructure. Besides LOM, Electron BackScatter Diffraction (EBSD) measurements have been performed at Central Facility of Electron Microscopy (GFE) in RWTH Aachen University to gain detailed information about the microstructure regarding grain size and shape, Euler angles, texture, angle between rolling direction and major axes of individual grains, afterwards referred to as slope, misorientation angle and substructures in terms of packets and blocks. The EBSD images in rolling direction (RD), transverse direction (TD) and in normal direction (ND) of the investigated pipeline steel X65 are displayed in Fig. 1b. Fig. 1c shows representatively the pole figures in three different directions visualizing the orientation of crystals (=texture) from the EBSD picture in RD. The maximum value in the pole figure represents the crystallographic preferred orientation, from which anisotropic material behavior can be concluded. The measurement field was 120 μm × 100 μm. The electron energy was 20 keV, while the step size between points was selected as 100 nm. These images will be used later to generate input data for RVEs.

### 3. Numerical modeling

#### 3.1. Crystal plasticity model

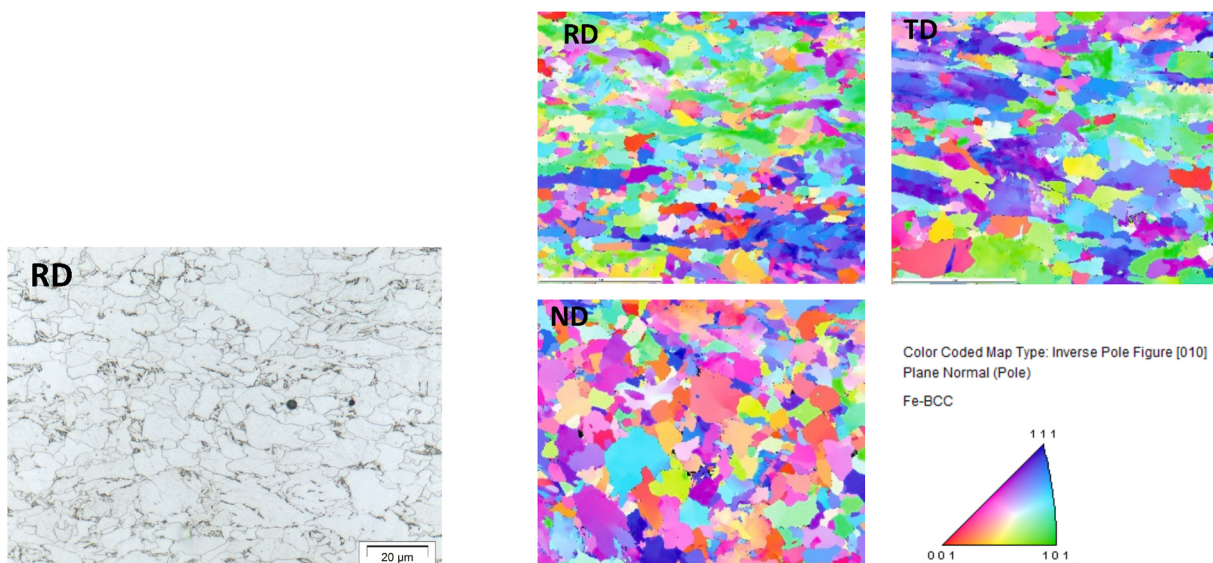
To consider the plastic material behavior of a single crystal on a microscopic level, a phenomenological crystal plasticity (CP) model based on dislocation slip mechanism was implemented according to Vajragupta et al. [37], which was then extended by the hydrogen diffusion to characterize possible weaknesses in the microstructure regarding hydrogen-induced damage. In the following, the fundamental equations of the CP model are summarized based on the work of Roters et al. [38].

The kinematics in the CP model were formulated through the multiplicative decomposition of the deformation gradient  $\mathbf{F}$  into an elastic  $\mathbf{F}^e$  and a plastic part  $\mathbf{F}^p$ , as shown in Eq. (1) [39]. The deformation gradient is a two-point-tensor that constitutes the transformation of an element from the reference to current configuration.

$$\mathbf{F} = \mathbf{F}^e \cdot \mathbf{F}^p, \quad (1)$$

With  $\mathbf{F} = \frac{\partial \mathbf{x}}{\partial \mathbf{X}}$ .  $\mathbf{X}, \mathbf{x}$  are position vectors, where capital and small letters represent the material (lagrangian) and spatial (eulerian) quantities, respectively.

Due to linearization of Eq. (1), one can get the additive decomposition of the strain tensor  $\boldsymbol{\epsilon}$  given in Eq. (2), which is applied in the small



(b) EBSD measurements.

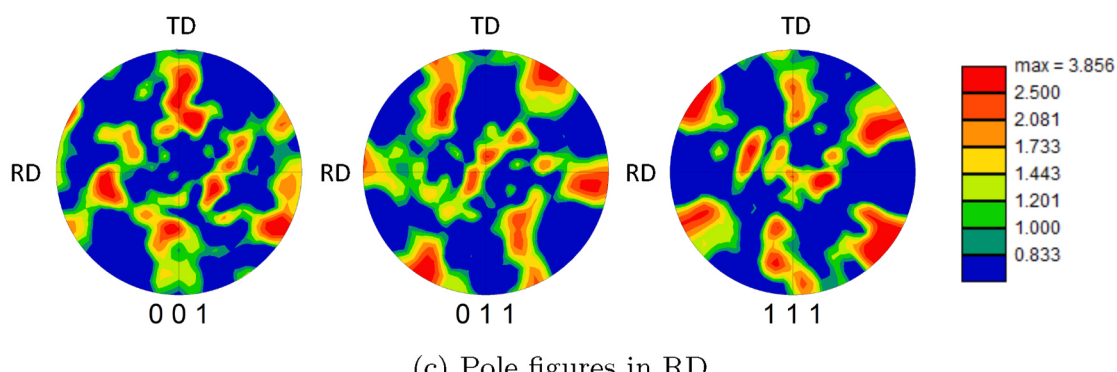


**Fig. 1.** (a) Light optical microscopy (LOM) analysis in rolling direction. (b) Electron backscatter diffraction (EBSD) measurements of X65 in three space directions with a scale of 45 μm. (c) The pole figures plot based on the EBSD image in RD.

strain theory.

$$\boldsymbol{\epsilon} = \boldsymbol{\epsilon}^e + \boldsymbol{\epsilon}^p \quad (2)$$

The evolution law of the plastic deformation gradient  $\mathbf{F}^p$  can be calculated based on the plastic velocity gradient  $\mathbf{L}^p$ , as given in Eq. (3) [38].

$$\dot{\mathbf{F}}^p = \mathbf{L}^p \cdot \mathbf{F}^p \quad (3)$$

The plastic velocity gradient  $\mathbf{L}^p$  describes the movement activities in all slip systems driven by (effective) shear rate  $\dot{\gamma}$  according to Eq. (4) [40].

$$\mathbf{L}^p = \sum_{\alpha=1}^{n_{\text{slip}}} \dot{\gamma}^\alpha \cdot [\mathbf{m}^\alpha \otimes \mathbf{n}^\alpha] \quad (4)$$

With  $\alpha$  as the corresponding slip system and  $n_{\text{slip}}$  as the number of (active) slip systems.  $\mathbf{m}^\alpha$  is the unit vector for the slip direction, while  $\mathbf{n}^\alpha$  stand for the unit vector normal to the slip plane.

Under the assumption of small elastic strains in the metal lattice the resolved shear stress  $\tau$  for a slip system  $\alpha$  can be simplified as in Eq. (5) [38].

$$\tau^\alpha = \mathbf{S} \cdot [\mathbf{m}^\alpha \otimes \mathbf{n}^\alpha], \quad (5)$$

where  $\mathbf{S}$  is the so-called 2.-Piola-Kirchhoff stress tensor. Application of this stress tensor provides the advantage to use Green-Lagrange strain tensor  $\mathbf{E}$  in further calculations.

The flow rule for a slip system  $\alpha$  can be expressed based on Schmid's law as follows [40,41]:

$$\dot{\gamma}^\alpha = \dot{\gamma}_0 \cdot \left| \frac{\tau^\alpha - \chi^\alpha}{\tau_c^\alpha} \right|^{p_{\text{Wf}}} \cdot \text{sgn}(\tau^\alpha - \chi^\alpha) \quad (6)$$

with  $\dot{\gamma}_0$  as the initial strain rate, which corresponds to a quasi-static loading in this work.  $p_{\text{Wf}}$  represents the strain rate sensitivity of the material.  $\tau_c^\alpha$  stands for the critical resolved shear stress that describes the slip resistance in a grain, while  $\chi^\alpha$  denotes the back stress.

The effect of another slipping system  $\beta$  on the strengthening response of slip system  $\alpha$  can be formulated, as given in Eq. (7) [42].

$$\tau_c^\alpha = q_{\alpha\beta} \cdot \underbrace{\left[ h_0 \cdot \left( 1 - \frac{\tau_c^\beta}{\tau_s} \right)^{p_{\text{Whd}}} \right]}_{\text{hardening matrix}} \cdot |\dot{\gamma}^\beta|, \quad (7)$$

where  $h_0$ ,  $p_{\text{Whd}}$ , and  $\tau_s$  are material constants describing the hardening behavior.  $q_{\alpha\beta}$  stands for a measure of latent hardening. Note that for bcc metals, such as the bainitic steel considered in this work, the critical resolved shear stress has to be modified due to the presence of non-planar propagation of screw dislocation cores during plastic deformation according to Vitek et al. [43], as shown in Eq. (8).

$$\tau_{c,\text{bcc}}^\alpha = \tau_c^\alpha - \Omega^\alpha \cdot \underbrace{\mathbf{S} \cdot [\mathbf{m}^\alpha \otimes \bar{\mathbf{n}}^\alpha]}_{\tau_{ng}^\alpha} \quad (8)$$

With  $\Omega^\alpha$  as a parameter indicating the net influence of non-slip stress on effective resistance and  $\tau_{ng}^\alpha$  as resolved shear stress on the non-slip plane with the normal  $\bar{\mathbf{n}}^\alpha$ .

Vajragupta [44] presented a Hall-Petch relation for the resolved shear stress  $\tau_c^\alpha$ , which is implemented in this work to formulate  $\tau_c^\alpha$  as a function of grain size.

$$\tau_c^\alpha = \tau_0 + \frac{k}{\sqrt{d}} \quad (9)$$

where  $\tau_0$  is the initial resolved shear stress,  $k$  is the Hall-Petch constant and  $d$  is the grain size.

The evolution law of the back stress  $\chi^\alpha$  on a slip system  $\alpha$  according to Frederik Armstrong type hardening [45] is given in Eq. (10).

$$\dot{\chi}^\alpha = A \cdot \dot{\gamma}^\alpha + B \cdot |\dot{\gamma}^\alpha| \cdot \chi^\alpha \quad (10)$$

with  $A$  and  $B$  as material parameters, that have to be calibrated under cycling loading.

Note that, the rate-dependent evolution laws in Eqs. (6), (7) and (10) must be discretized in time to be implemented in a finite element framework.

### 3.2. Hydrogen diffusion model

In the following the implementation of hydrogen diffusion model is briefly presented according to the theory introduced by Oriani [46]. The governing equations were summarized based on the work of Sofronis and McMeeking [47] and Barrera et al. [48], who presented a hydrogen diffusion model in the crack tip and a 2d hydrogen diffusion model coupled with macromechanical elasto-plastic material behavior, respectively. Based on the assumptions made by Oriani [46], the total hydrogen concentration  $C_T$  in the metal lattice can be written as a sum of the hydrogen concentration in the interstitial lattice sites  $C_L$  and in so-called hydrogen traps (=lattice defects)  $C_X$ , such as grain boundaries, dislocations, carbides, non-metallic inclusions.

The total hydrogen concentration can be expressed as:

$$\widehat{C}_{T(\text{total})} = \widehat{C}_{L(\text{lattice})} + \sum_{i=1}^{n_{\text{traps}}} \widehat{C}_X^i \quad (11)$$

Note that in this study, the symbols labeled with  $(\widehat{\bullet})$  represent molar quantities.

The hydrogen concentration in interstitial lattice sites can be calculated as given in Eq. (12) [47].

$$\widehat{C}_L = \xi \cdot \vartheta_L \cdot \widehat{N}_L, \quad (12)$$

where  $\xi$  stands for the number of interstitial lattice sites per solvent atom.  $\vartheta_L \in [0, 1]$  represents the occupancy level of lattice sites.  $\widehat{N}_L$  denotes the mol of solvent per unit volume [48].

$$\widehat{N}_L = \rho / A_R \quad (13)$$

With  $\rho$  as the density and  $A_R$  as lattice element's relative atomic mass.

In analogy to Eq. (12), the trapped hydrogen concentration on dislocation side can be determined as follows [47];

$$\widehat{C}_X^d = \zeta^d \cdot \vartheta_X^d \cdot \widehat{N}_X^d (\bar{\epsilon}^p), \quad (14)$$

where  $\zeta^d$  indicates the number of trapping sites, while  $\vartheta_X^d \in [0, 1]$  stands for the occupancy level of trapping sites.  $\widehat{N}_X^d$  describes the dislocation trap density as a function of plastic strain  $\bar{\epsilon}^p$ . For a bcc lattice  $N_X^d$  can be formulated according to Kumnick and Johnson [49] as shown in Eq. (15).

$$\log(N_X^d(\bar{\epsilon}^p)) = 23.26 - 2.33 \cdot \exp[-5.5 \cdot \bar{\epsilon}^p] \quad (15)$$

Note that to get molar values  $N_X^d$  has to be divided by the Avogadro constant  $N_A$  in further calculations.

In addition to dislocations, grain boundaries and carbides were implemented as hydrogen traps according to Dadfarnia et al. [50], who assumed constant trap densities for grain boundaries  $\widehat{N}_X^{gb}$  and carbides  $\widehat{N}_X^c$ . The hydrogen concentration in grain boundaries  $\widehat{C}_X^{gb}$  and carbides  $\widehat{C}_X^c$  can be calculated based on Eqs. 16 and 17.

$$\widehat{C}_X^{gb} = \zeta^{gb} \cdot \vartheta_X^{gb} \cdot \widehat{N}_X^{gb} \quad (16)$$

$$\widehat{C}_X^c = \zeta^c \cdot \vartheta_X^c \cdot \widehat{N}_X^c \quad (17)$$

In analogy to the dislocations  $\zeta^{gb}$  and  $\zeta^c$  denote the number of trapping sites for grain boundaries and carbides, while  $\vartheta_X^{gb} \in [0, 1]$  and  $\vartheta_X^c \in [0, 1]$  stand for the occupancy level of the corresponding trapping sites.

Oriani [24,46] postulated the equilibrium condition between the hydrogen atoms resolved in interstitial lattice sites and trapping sites under the assumption of  $\vartheta_L \ll 1$ .

$$\frac{\vartheta_X^i}{1 - \vartheta_X^i} = \frac{\vartheta_L}{1 - \vartheta_L} \kappa_X^i \quad (18)$$

with  $\kappa_X^i$  as equilibrium constant per trap  $i$  defined as:

$$\kappa_X^i = \exp \left[ -\frac{B_E^i}{R_{\text{gas}} \cdot T_0} \right], \quad (19)$$

where  $B_E^i < 0$  is the binding energy per trap  $i$ ,  $R_{\text{gas}}$  is the gas constant and  $T_0$  is the (room) temperature.

The equilibrium condition leads to formulation of hydrogen concentration in traps as a function of hydrogen concentration in interstitial lattice sites. The final form of the hydrogen diffusion equation is displayed in Eq. (20).

$$\begin{aligned} \widehat{C}_T(\widehat{C}_L, \overline{\varepsilon}_n^p, \sigma_h) = & \underbrace{\widehat{C}_{L,n-1} \cdot \exp \left( \sigma_h \cdot \frac{V_H}{R_{\text{gas}} \cdot T_0} \right)}_{\text{effect of hydrostatic stress}} + \\ & \underbrace{\widehat{N}_X^d(\overline{\varepsilon}_n^p) \cdot \frac{\zeta^d \cdot \kappa_X^d \cdot \widehat{C}_{L,n-1}}{\xi \cdot \widehat{N}_L + \kappa_X^d \cdot \widehat{C}_{L,n-1}}}_{\text{effect of plastic strain via dislocations}} + \underbrace{\widehat{N}_X^{gb} \cdot \frac{\zeta^{gb} \cdot \kappa_X^{gb} \cdot \widehat{C}_{L,n-1}}{\xi \cdot \widehat{N}_L + \kappa_X^{gb} \cdot \widehat{C}_{L,n-1}}}_{\text{effect of grain boundaries}} + \\ & \underbrace{\widehat{N}_X^c \cdot \frac{\zeta^c \cdot \kappa_X^c \cdot \widehat{C}_{L,n-1}}{\xi \cdot \widehat{N}_L + \kappa_X^c \cdot \widehat{C}_{L,n-1}}}_{\text{effect of carbides}} \end{aligned} \quad (20)$$

With  $\sigma_h$  as the hydrostatic stress and  $V_H$  as partial molar volume of hydrogen. Eq. (20) enables the possibility to calculate the hydrogen concentration in a steady state condition based on the state variables from crystal plasticity model. However, it is noteworthy that Eq. (20) does not include the effects of inclusions on hydrogen trapping by strain fields at inclusion interfaces. To overcome this problem Peng et al. introduced an additional term to calculate hydrogen concentration depending on the critical inclusion length [51].

The crystal plasticity model was implemented in Abaqus/Implicit as a UMAT subroutine using finite strain theory, while the hydrogen diffusion model was implemented as a USDFLD subroutine, where the temperature field was interpreted as hydrogen concentration. It is noteworthy that, due to the internal structure of Abaqus, USDFLD subroutine is called after the UMAT subroutine. That leads to the fact that,

the hydrogen concentration is calculated based on values from previous time increment  $t_{n-1}$ . However, in case of a small time increment  $dt$  the error is negligible.

#### 4. RVE generation

The statistical representative volume elements (RVEs) used in this work were generated applying the in-house software DRAGen (Discrete Representative Volume Element Automation and Generation) [52–55]. Fig. 2 summarizes the general procedure of RVE generation.

The RVE generator DRAGen needs as an input statistical data regarding microstructure characteristics, such as grain size, texture, slope, misorientation angle and substructures. For this purpose, EBSD measurements were performed. To extract the data of interest from the pole figures MATLAB toolbox MTEX was utilized [56].

As presented by Pütz et al. [53], generative adversarial networks with Wasserstein metric were employed to create statistically equivalent synthetic datasets obtained from real microstructure via MTEX to generate geometrically different but statistically identical RVEs. Since the microstructure is not the same at every point in the material and exhibits deviations. Based on the generated statistical data, the grains were placed in the volume using a random sequential addition algorithm (RSA) [57,58]. Note that grains were approximated as ellipsoids based on the work of Mulchrone and Choudhury [59]. To achieve 100 % volume filling, the placed grains were first shrunk and then grown based on a discrete Voronoi tessellation, as presented by Henrich et al. [52]. In the next step optionally substructures can be created in each grain [55]. Fehlemann et al. [54] extended DRAGen to consider inclusions and voids in RVE. Note that inclusions were also approximated as ellipsoids. For this reason, in this work the contour of the inclusions was detected from metallographic investigations with a self-written Python script and approximated as an ellipsoid. The needed input parameters semi-major axis and semi-minor axis were automatically determined and passed to DRAGen. Fig. 3a illustrates exemplarily the results of contour detection and geometry approximation in case of two inclusions. Note that the inclusions measurements were performed layer by layer to get the exact thickness. In the final step the RVE was meshed using the mesh generator implemented in DRAGen to run simulations with Abaqus. The element type was C3D8 (3d continuum brick element with eight nodes). To validate the RVEs, Fig. 3b–e depict representatively the grain size distribution with respect to the input and output data, the grain shape with respect to aspect ratio (AR) and slope as a pairplot, the comparison between the measured and predicted texture, as well as the selected phase fraction for matrix and inclusions. From Fig. 3b–e, it can be concluded that the created RVEs can reproduce the grain size and shape as well as the texture with reasonably high accuracy. Note that the

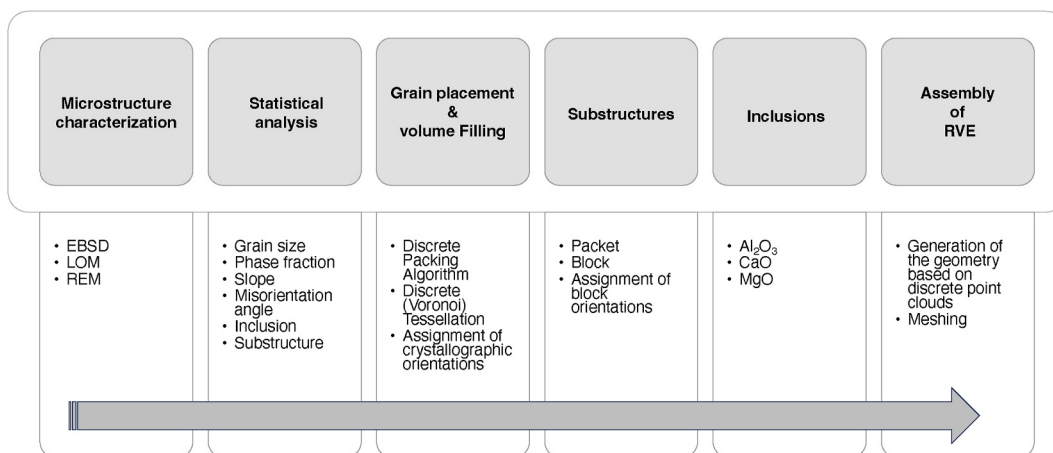
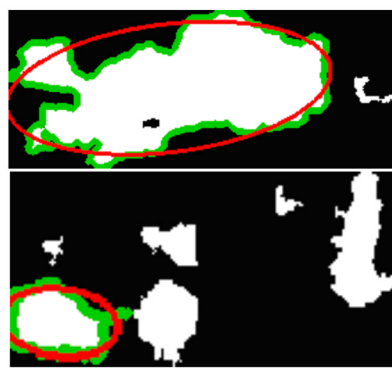
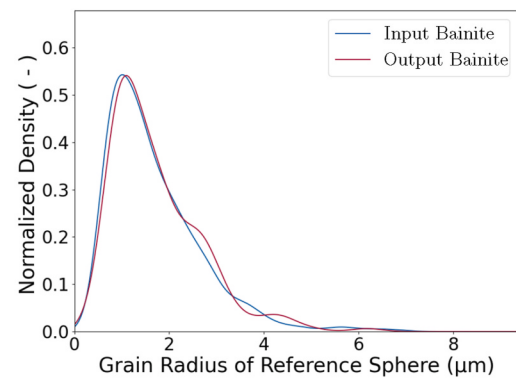


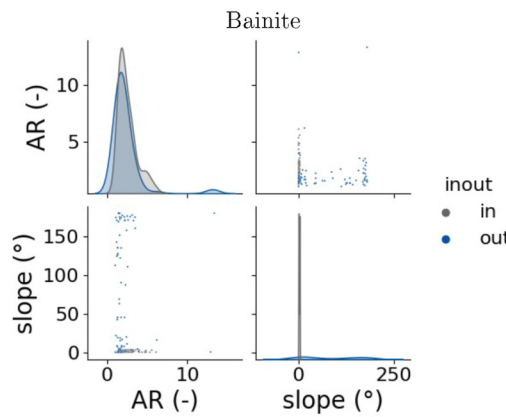
Fig. 2. Flowchart of the RVE generation procedure with in-house software DRAGen.



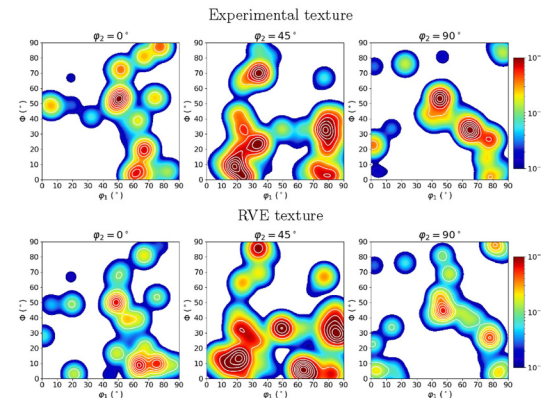
(a) Geometry approximation.



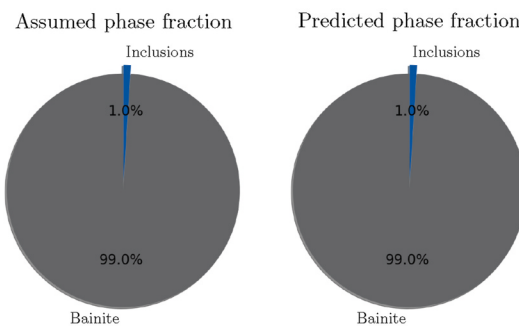
(b) Comparison of grain size distribution.



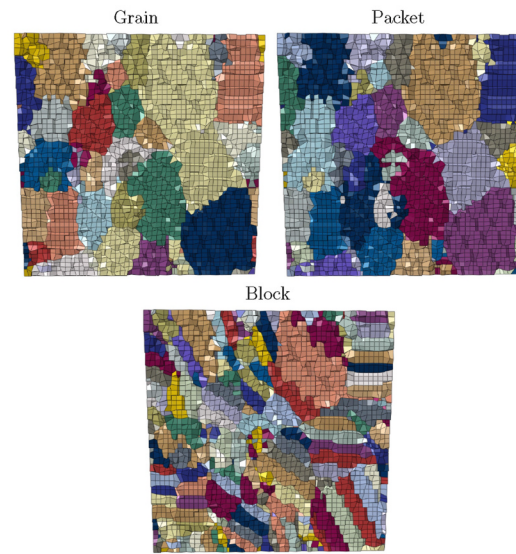
(c) Grain shape control.



(d) Experimental and RVE textures.



(e) Phase fraction.



(f) Exemplarily depiction of the substructures in each grain as packets and blocks.

**Fig. 3.** Approximated inclusions geometry as ellipsoids (a) as well as representative validation of the generated RVEs regarding grain size distribution (b), grain shape (c), texture (d), adjusted phase fraction between matrix and inclusions (e) and substructures (f).

texture prediction is conducted to the size of the RVE and the corresponding number of grains. The more grains, the higher the agreement with the experiment but the higher the computational cost.

**Fig. 3f** shows exemplarily the generated substructure for bainite with respect to packets and blocks. For the visualization of substructures, the RVE was cut through into two parts. In this example, it can be seen that a packet has been assigned for each grain and each packet consists of many blocks with corresponding orientations. Noteworthy, their contraction is based on the Kurdjumov-Sachs (K-S) orientation relationship.

## 5. Results and discussion

### 5.1. Calibration of crystal plasticity model

The crystal plasticity model was calibrated based on the engineering strain vs. engineering stress curve from a (mesoscopic) quasi-static uniaxial tensile test. For this purpose, three RVEs with substructures were generated. Furthermore, so-called periodic boundary conditions were applied to the RVEs using node-coupling technique [60,61], representing the uniaxial tension load.

Eng. stresses and eng. strains were averaged across the RVEs under the consideration of grain size based on Eq. (21), where  $(\bullet)_{22}$  is the loading direction. It should be noted that in this calibration procedure the ferritic-bainitic microstructure is homogenized for simplicity. Since the focus of this work is primarily on investigating the influence of non-metallic inclusions on hydrogen diffusion, the effects of the different phases are not investigated.

$$\begin{aligned}\tilde{\sigma}_{eng,RVE} &= \sum_j^{n_{grain}} \tilde{\sigma}_{22}^j \frac{V^j}{V_{RVE}} \\ \tilde{\epsilon}_{eng,RVE} &= \sum_j^{n_{grain}} \tilde{\epsilon}_{22}^j \frac{V^j}{V_{RVE}}\end{aligned}\quad (21)$$

With  $V^j$  as the volume  $j$ -th grain and  $V_{RVE}$  as RVE volume.

**Fig. 4** displays the experimental eng. stress vs. eng. strain curve from the uniaxial tensile test (solid line) as well as the predictions of the iteratively calibrated CP model. Since each RVE looks from geometrical point of view slightly different, even though they are all based on the same statical distribution functions derived from the EBSD measurements, the model parameters were validated on additional RVEs

regarding their robustness. Thus, RVE0 was used to calibrate the model parameters, while RVE1 and RVE2 served as validation. From **Fig. 4** a very good agreement between simulation and experiment can be obtained for all RVEs.

The calibrated parameters of the crystal plasticity model for X65 pipeline steel are listed in **Table 2**. The parameters  $C_{11}$ ,  $C_{12}$  and  $C_{44}$  represent the elastic material constants. It is noteworthy that the parameters  $A$  and  $B$  in the model were related to the kinematic hardening. Since cyclic loading, e.g. in terms of fatigue analyses, was not investigated in this study, these parameters were neglected. The hardening due to grain refinement was taken into account in the implemented model via Hall-Petch relationship. Since the authors calculated the stresses and strains as an average value regarding grain size/volume, as shown in Eq. (21), it was not necessary to calibrate the Hall-Petch parameter  $k$  additionally. Note that the number of slip systems for bcc is  $n_{slip} = 48$ . However, due to the faced convergence problems during the implicit time integration scheme in Abaqus and high computational cost, the authors considered  $n_{slip} = 12$  on the  $\{1\ 1\ 0\}$  slip plane and in  $<1\ 1\ \bar{1}>$  slip direction. Since the crystal plasticity model is rate dependent, the

**Table 2**

Summary of the material parameters of crystal plasticity (CP) and hydrogen diffusion models for X65 as well as the thermo-mechanical properties for X65 and non-metallic inclusion  $\text{Al}_2\text{O}_3$ .

CP Parameters	Hydrogen Parameters [48, 50]	Thermo-mechanical parameters
$C_{11} = 231 \text{ GPa}$	$\hat{N}_L = 9.24E19 \text{ mol/mm}^3$	$\rho_{X65} = 7.85E-9 \text{ ton/mm}^3$
$C_{12} = 134.7 \text{ GPa}$	$N_A = 6.023E23 \text{ atoms/mol}$	$E_{X65} = 210 \text{ GPa}$
$C_{44} = 114.4 \text{ GPa}$	$\xi = 6$	$\nu_{X65} = 0.3$
$n_{slip} = 12$	$V_H = 2E3 \text{ mm}^3/\text{mol}$	$K_{X65} = 52 \text{ W/(mK)}$
$p_{w\eta} = 20$	$T = 293.15 \text{ K}$	$C_p_{X65} = 4.80E9 \text{ mJ/(tonK)}$
$\dot{\gamma}_0 = 0.001 \text{ 1/s}$	$R_{\text{gas}} = 8314.4621 \text{ mJ/(K mol)}$	$\delta_{X65} = 11E-6 \text{ 1/K}$
$h_0 = 350 \text{ MPa}$	$B_E^d = -18E6 \text{ mJ/mol}$	$\rho_{\text{Al}_2\text{O}_3} = 3.95E-9 \text{ ton/mm}^3$
$\tau_0 = 195 \text{ MPa}$	$B_E^{gb} = -58.6E6 \text{ mJ/mol}$	$E_{\text{Al}_2\text{O}_3} = 394 \text{ GPa}$
$\tau_s = 824.66 \text{ MPa}$	$B_E^c = -11.5E6 \text{ mJ/mol}$	$\nu_{\text{Al}_2\text{O}_3} = 0.21$
$k = 0$	$\xi^{cd} = 1$	$K_{\text{Al}_2\text{O}_3} = 30 \text{ W/(mK)}$
$p_{whd} = 2.97$	$\xi^{gb} \cdot N_X^{gb} = 8.464E13 \text{ sites/mm}^3$	$C_p_{\text{Al}_2\text{O}_3} = 880E9 \text{ mJ/(tonK)}$
$A = 0$		$\delta_{X65} = 8.1E-6 \text{ 1/K}$
$B = 0$		

$\rho$ : Density,  $E$ : Young's modulus,  $\nu$ : Poisson's ratio,  $K$ : Conductivity.  
 $C_p$ : Specific heat,  $\delta$ : Thermal expansion coefficient.

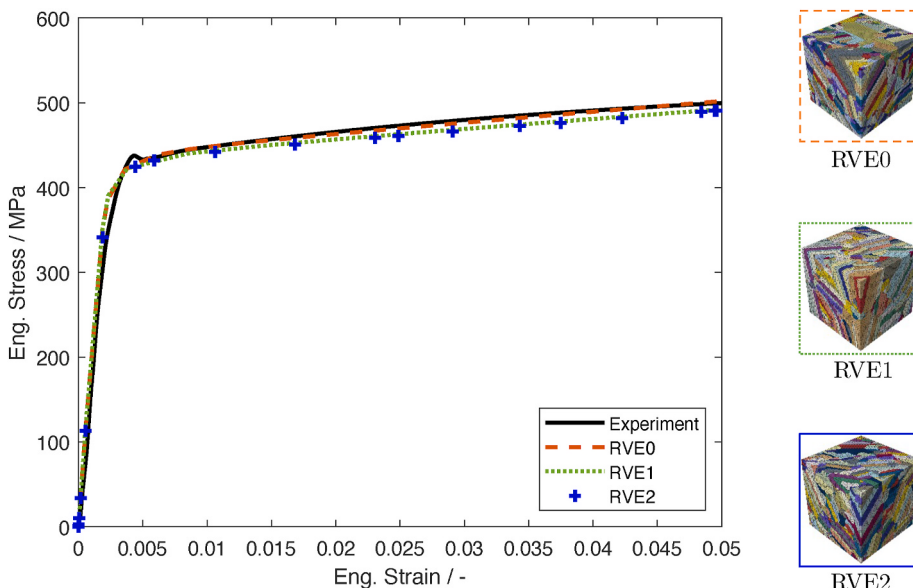


**Fig. 4.** Calibration and validation of the CP model based on the uniaxial tensile test. The CP parameters were calibrated on RVE0 and validated on RVE1 and RVE2.

step time should be chosen appropriately high to assume quasi-static loading condition in the simulation during parameter identification.

## 5.2. Influence of non-metallic inclusions on hydrogen diffusion

The driving force for hydrogen diffusion is the hydrostatic part of the external as well as internal/residual stresses. In this work, the focus lies on the latter. To study the influence of complex microstructural effects on hydrogen distribution, it is necessary to introduce these driving forces into the microstructure. In this work both thermally and mechanically induced (hydrostatic) stresses are investigated. First, a 3d RVE composed of 631 grains and 1 % inclusion volume fraction was created and meshed with the element type C3D8T (see Fig. 5a). In this study, the chemical composition of inclusions is assumed to be  $\text{Al}_2\text{O}_3$ . Since it is reported in the literature that  $\text{Al}_2\text{O}_3$  is one of the most critical inclusions regarding hydrogen-induced-cracking [62–64]. Second, to generate residual stresses, a cooling processes from 996.15 K to room temperature 293.15 K was simulated, where elastic material behavior was assumed for the inclusions and CP model was applied for the grains. This step can be interpreted as the cooling procedure of the material after hot rolling prior to pipe forming [65]. Note that these thermal residual stresses after cooling are induced due to inhomogeneous deformation resulting from different thermal properties of the matrix and inclusions (see Table 2), where the (ratio of) thermal expansion coefficient is the decisive parameter. Third, to model hydrogen diffusion, the model used in the cooling simulation was duplicated, and the residual stresses from the cooling model were employed as the initial stress state. Since the temperature degree of freedom was rewritten as a hydrogen field, model duplication was necessary to perform the simulation with Abaqus/Implicit. Fourth, an initial homogeneously distributed hydrogen concentration was applied on the RVE surface  $\hat{C}_{L0} = 3.57 \times 10^{-8} \text{ mol/mm}^3$ . In the last step, hydrogen diffusion was simulated based on the thermal residual stresses.

Fig. 5 displays the simulation results in terms of thermally induced residual stresses in RVE after cooling, the distribution of hydrostatic stresses around the inclusions as well as the accumulation of hydrogen atoms according to the residual stresses. Fig. 5b shows the stress state in terms of von Mises stresses in the RVE at the end of the cooling step due to shrinking of the matrix on the non-metallic inclusions. The localized stress distribution due to the different thermal expansion coefficients

between matrix and inclusion hints at where the non-metallic inclusions are positioned. The maximum stress is obtained in the vicinity of the inclusion and is 1026 MPa. Similar to the von Mises stress distribution, hydrostatic stresses are also generated around the inclusions (see 5c). Hydrostatic part of the residual stresses leads to the expansion of the metal lattice so that hydrogen atoms accumulate surrounding the inclusions according to Eq. (20), in which the hydrostatic stresses are the driving force for hydrogen diffusion (see Fig. 5d,e,f). As the number of hydrogen atoms tapped around the inclusions increases, the probability of hydrogen atoms recombining to form hydrogen molecules increases. Since the hydrogen molecules occupy much more space than the hydrogen atoms, the internal pressure increases, leading to the initiation of microcracks. From a damage initiation perspective, based on these results, non-metallic inclusions serve as irreversible hydrogen traps with high binding energy [66] through the shrinking phenomenon of the matrix and imply a weakness in the microstructure as the hydrogen concentration reaches a maximum. In addition, the micro-voids located in the interface of matrix and inclusion serve as hydrogen traps [64]. Hence, hydrogen-induced cracks will initiate from inclusion sites. These conclusions are in good agreement with the experimental findings from literature [62–64,67–69]. The simulation results presented here are also consistent with the numerical study conducted by Peng et al. [70], who investigated the effects of non-metallic inclusions on hydrogen diffusion in APL X70 steel. They also observed a localized stress field around the inclusions caused by cooling after hot forming. Since it is difficult to obtain an overview of the local hydrogen amount in each grain from the 3d RVE, Fig. 5g additionally plots the probability density of the averaged total hydrogen concentration per each grain in the RVE at the end of the simulation, while Fig. 5h presents the total hydrogen concentration per element. Latter graph is useful to visualize the critical local peaks that disappear when considering the mean values over a grain. Since a grain consists of many elements. From these distribution functions, it can be deduced that most grains have a hydrogen concentration on the order of  $4.2 \times 10^{-8} \text{ mol/mm}^3$ , which is around 18 % higher than the initial concentration. Note that during the simulations hydrogen atoms are not allowed to diffuse through the non-metallic inclusions. The numerical results presented in this section support the conclusion that the HIC resistance of steels can be increased by reducing the level of impurities, as the critical local peaks of hydrogen concentration, leading to micro-crack initiation, are prevented. This statement is in good agreement with the results presented by Huang et al. who showed that the HIC

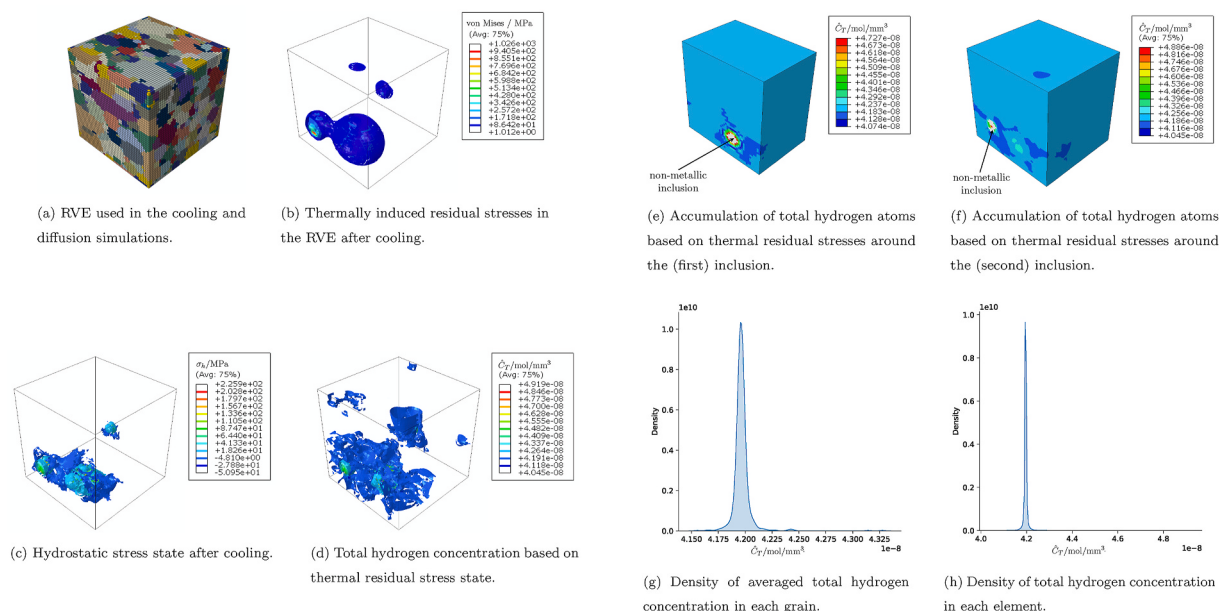


**Fig. 5.** Visualization of thermal internal stress state and hydrostatic stresses after cooling and hydrogen concentration after diffusion.

sensitivity becomes higher with an increasing number of non-metallic inclusions [62]. In addition, a low impurity level leads to a decrease in the number of possible hydrogen traps in the metal lattice, where hydrogen atoms can accumulate and combine to hydrogen molecules, leading to an increase in hydrogen pressure and thus to crack initiation.

The model parameters used for the hydrogen diffusion model were adapted from Refs. [48,50] (see Table 2).

### 5.3. Influence of stress state on hydrogen diffusion

To investigate the effect of stress state on hydrogen diffusion on microscopic level the RVE from Sec. 5.2 was loaded under uniaxial tension, shear, plain strain and biaxial tension. The applied periodic boundary conditions are displayed in Fig. 6. These idealized boundary conditions can help to reproduce similar local stress fields as, for example, in different pipe forming steps and give an idea of critical points in the pipe.

Similar to the performed simulation in Sec. 5.2, a two-step model was built. In the first step the RVE was mechanically loaded. In the second step, uniformly distributed hydrogen concentration was applied on the RVE surface and hydrogen diffusion was modeled based on the mechanically induced internal stresses. As boundary conditions the initial hydrogen concentration was selected as  $\hat{C}_{I0} = 3.57 \times 10^{-8} \text{ mol/mm}^3$  and 5 % ( $u = 1.5 \mu\text{m}$ ) total elongation was applied. Fig. 7 shows the total hydrogen concentration at different stress states for both RVEs with (b, d, f, g) and without (a, c, e, g) inclusions. Note that RVEs are cross-sectioned to illustrate the hydrogen concentration around inclusions. From Fig. 7, it can be seen that the RVEs with non-metallic inclusions achieve higher local hydrogen concentrations under uniaxial, biaxial and plain strain loading conditions, with the maximum at the inclusion-matrix interface. The largest spatial deviation due to the presence of inclusions was reached under uniaxial tension with +28 %, followed by plain strain with +26 % and biaxial tension with +18.5 %. However, for the RVE with inclusions, a decrease of -6 % in peak hydrogen concentration was observed under shear loading. The higher local hydrogen concentration due to the non-metallic inclusions can be explained by the increased local hydrostatic stresses and plastic strains in the RVE through the notched effect. Fig. 8 illustrates exemplarily the effect of non-metallic inclusions on hydrostatic stress and plastic strain distribution in the microstructure under 5 % biaxial tension. It can be seen that a 50 % increase in hydrostatic stress and a 60 % increase in plastic strain were obtained locally in the RVE with non-metallic inclusions. However, it should be noted that the results may vary depending on the chemical composition and aspect ratio of the inclusions, as Peng et al. showed that MnS (soft-phase) has a much larger HIC nucleation size than harder inclusion (TiO) [51].

Furthermore, from Fig. 7 one can also observe that the hydrogen concentration at the end of the simulation is not homogeneously distributed in the RVEs. This can be explained by the grain anisotropy considered in the CP model and resulting direction-dependent plastic strain and hydrostatic stress evolution in the microstructure as displayed in Fig. 8.

To focus on the influence of stress state, the microstructure simula-

tion results without non-metallic inclusions were analyzed. From Fig. 7 (a, c, e, g) one can read that the highest local hydrogen concentration is reached under biaxial tension followed by plain strain, shear loading and uniaxial tension. The maximum deviation lies around 11 % between biaxial and uniaxial tension. To have a better understanding of the influence of stress state on hydrogen diffusion, Fig. 9 summarizes (for easy readability) the averaged stress triaxiality, Lode angle parameter, hydrostatic stress, plastic strain, as well as the total hydrogen concentration per grain in the RVEs at different stress states as a pairplot. The probability density of each quantity is given on the diagonal. Pairplots are commonly used to determine or visualize possible correlations between different state variables. From Fig. 9 a clear correlation between hydrostatic stress respectively stress triaxiality and total hydrogen concentration can be seen as hydrogen concentration increases with increasing hydrostatic stress. Since hydrostatic stress is the main influence for the local hydrogen concentration this relation can be taken as trivial. The effect of plastic strain is considered in the dislocation trap density  $N_X^d(\bar{\varepsilon}_p)$ . However, the link between plastic strain and hydrogen concentration seems not to be as pronounced as in case of hydrostatic stress. This can be explained by the fact that  $N_X^d(\bar{\varepsilon}_p)$  converges to a constant value with increasing plastic strain, whereby the converged value is reached at a plastic strain of 0.7. It is evident from Fig. 9 that there are many grains for which plastic strain values higher than 0.7 are predicted in all loading cases, which more or less “neutralizes” the influence of plastic strain on hydrogen diffusion when comparing different stress states. However, it can be concluded that under biaxial tension the highest (local) plastic strain values are reached followed by plain strain, uniaxial tension and shear. This means the dislocation density in the RVEs also shows the same tendency. Therefore, the contribution of  $\hat{C}_X^d$  is most pronounced under biaxial loading and comparatively less pronounced under shear loading. For the local hydrostatic stress distribution in the RVE, the same order as plastic strains is observed. In analogy to  $\hat{C}_X^d$ , it can be deduced that the contribution of  $\hat{C}_L$  is the highest under biaxial loading. Note that the contribution of hydrogen atoms from trapping sites at grain boundaries  $\hat{C}_X^{gb}$  and carbides  $\hat{C}_X^c$  is considered in the total hydrogen concentration  $\hat{C}_T$ . However, the trapping densities  $\hat{N}_X^{gb}$  and  $\hat{N}_X^c$  are considered as constant values according to the literature [50,71,72], which leads to the fact that independently of the investigated loading conditions or stress states, the values for  $\hat{C}_X^{gb}$  and  $\hat{C}_X^c$  will be the same. Thus, the effect of stress state on  $\hat{C}_X^{gb}$  ( $= 1.405 \times 10^{-10} \text{ mol/mm}^3$ ) and  $\hat{C}_X^c$  ( $= 6.076 \times 10^{-9} \text{ mol/mm}^3$ ) is not presented in this study. From the results of these RVE simulations, it can be concluded that the local maximum hydrostatic stresses and plastic strains to which the grains are subjected determine the critical location with maximum hydrogen concentration in the microstructure where the microcracks can initiate and grow under sustained loading and lead to failure. These findings are in good agreement with the experimental results reported in literature [73–75].

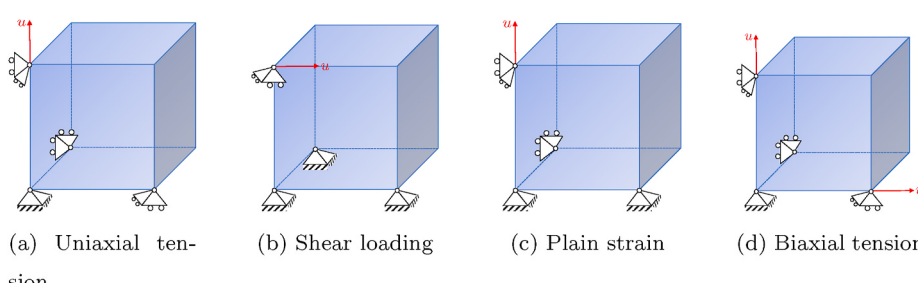
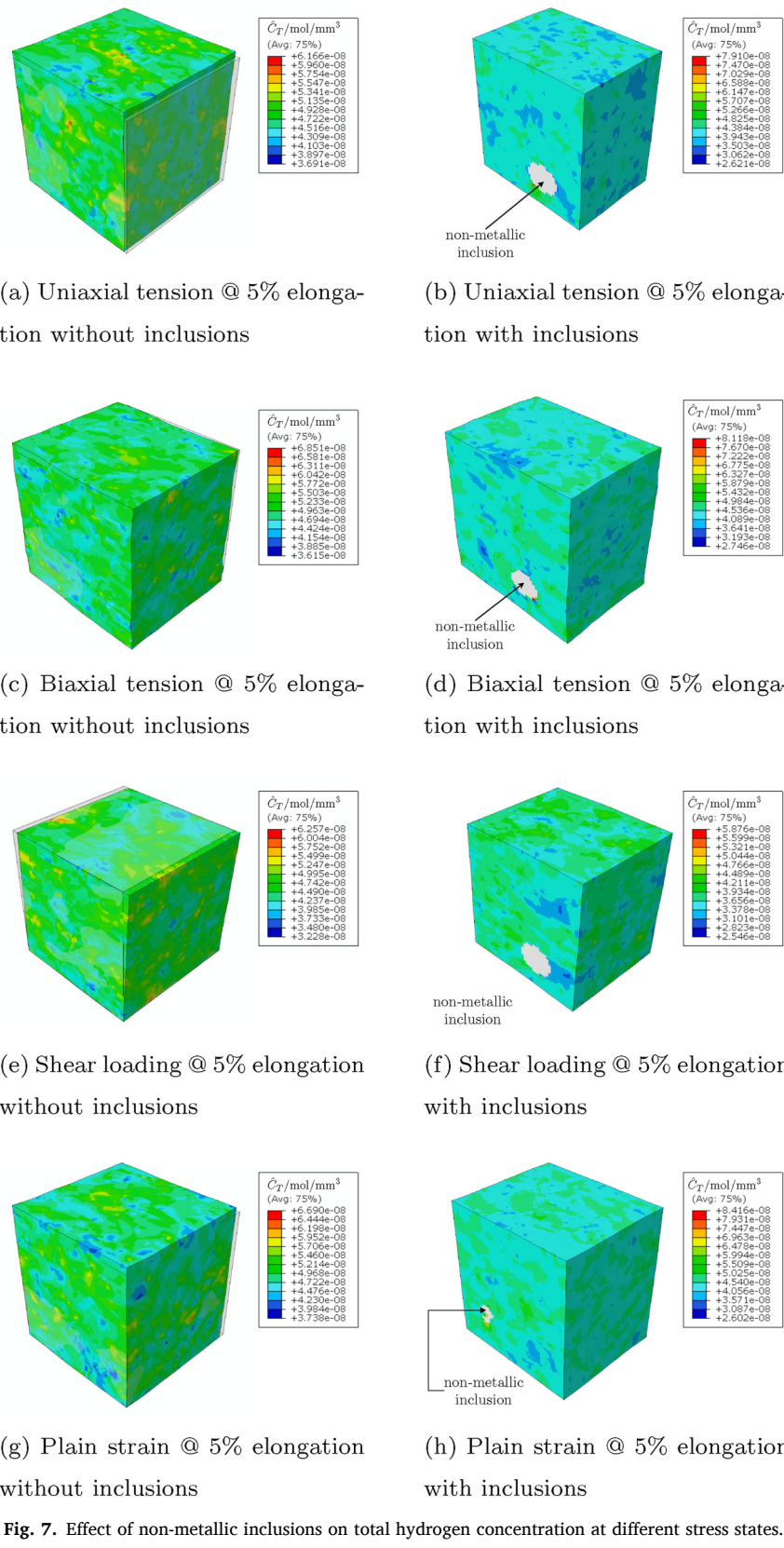


Fig. 6. Periodic boundary conditions for different stress states.



**Fig. 7.** Effect of non-metallic inclusions on total hydrogen concentration at different stress states.

## 6. Conclusion

In this study a phenomenological crystal plasticity model was implemented and coupled with hydrogen diffusion to investigate the influence of microstructural heterogeneities including non-metallic

inclusions based on thermally and mechanically induced residual stresses at different stress states. The finding are as follows:

- Non-metallic inclusions affect the hydrogen susceptibility of pipeline steels in two ways, namely as a notch effect (pronounced under

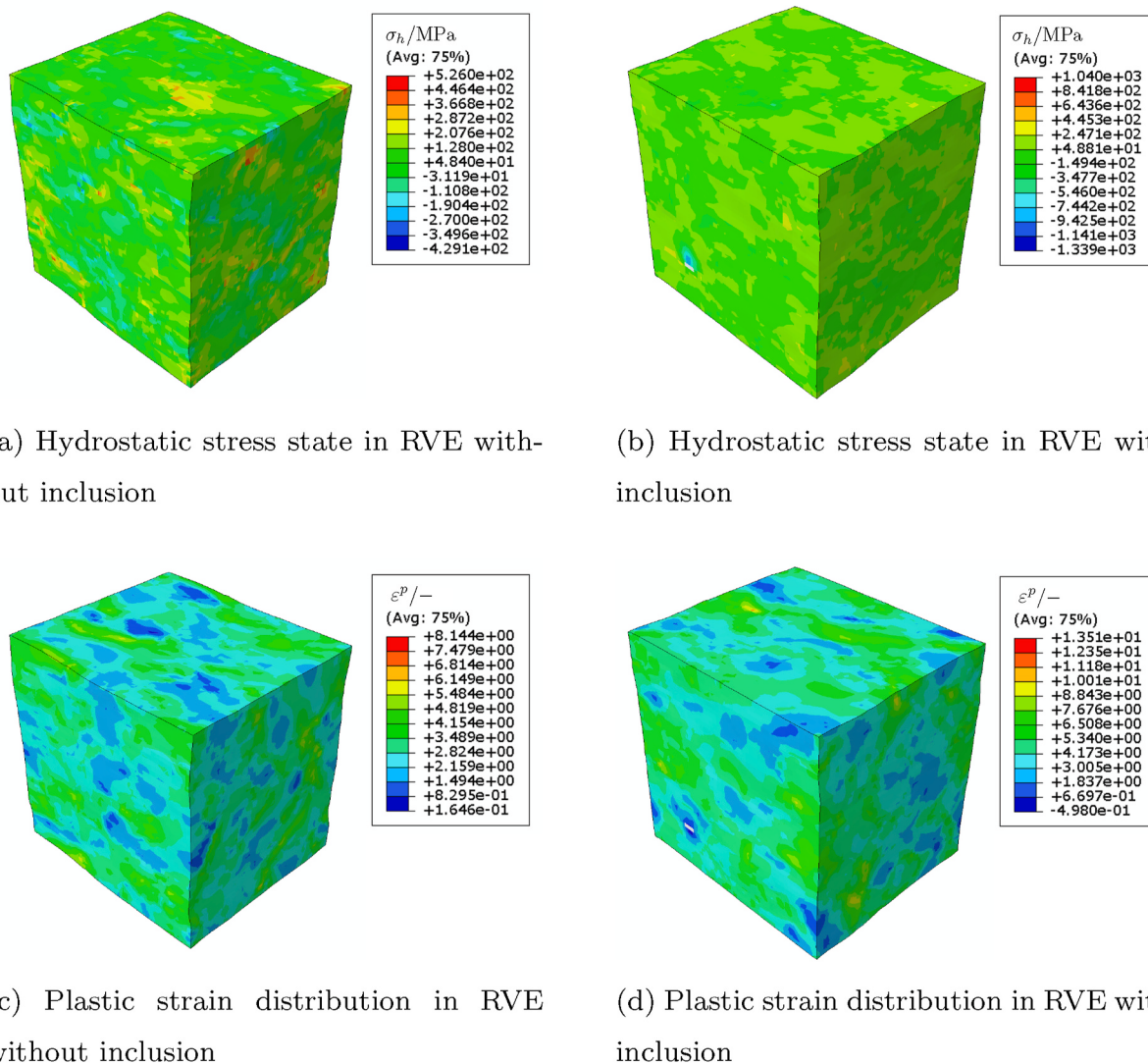


**Fig. 8.** Comparison of the distribution of hydrostatic stress (a,b) and plastic strain (c,d) in RVEs with and without inclusion under 5 % biaxial tension.

mechanical loading) and as a contributor to residual stresses (pronounced under thermal loading in terms of a cooling process).

- The effect of matrix shrinkage on the inclusions and the resulting residual stress field, based on a cooling process after hot rolling, leads to the accumulation of hydrogen atoms around the inclusions, resulting in locally high critical concentrations.
- The presence of non-metallic inclusions leads due to the notch effect to higher local hydrogen concentrations under uniaxial tension (+28 %), plain strain (+26 %) and biaxial tension (+18.5 %). Under shear loading however, the opposite is observed (-6 %).
- Local peak of the hydrogen concentration in the microstructure depends on the stress state. Maximum local hydrogen concentration is observed under biaxial tension, while the minimum concentration is obtained under uniaxial tension. The difference between maximum and minimum concentration is around 11 %.
- The resistance against hydrogen-induced-cracking can be increased by decreasing the level of impurities.

As an outlook, the extension of the presented microscale model to the mesoscale considering a coupled chemical-mechanical damage model as a function of stress state can be given.

#### Author contributions

Conceptualization B.T.; methodology, B.T. and M.D.; software, B.T., M.D.; validation, B.T.; resources, M.D. and S.M.; data curation, S.M.; writing—original draft preparation, B.T.; writing—review and editing, M.D. and S.M.; visualization, B.T.; supervision, M.D., S.M.; funding acquisition, S.M. All authors have read and agreed to the published version of the manuscript.

#### Funding

This project was co-funded by the European Union under grant no 101112571.



#### Declaration of competing interest

The authors declare that they have no known competing financial interests or personal relationships that could have appeared to influence

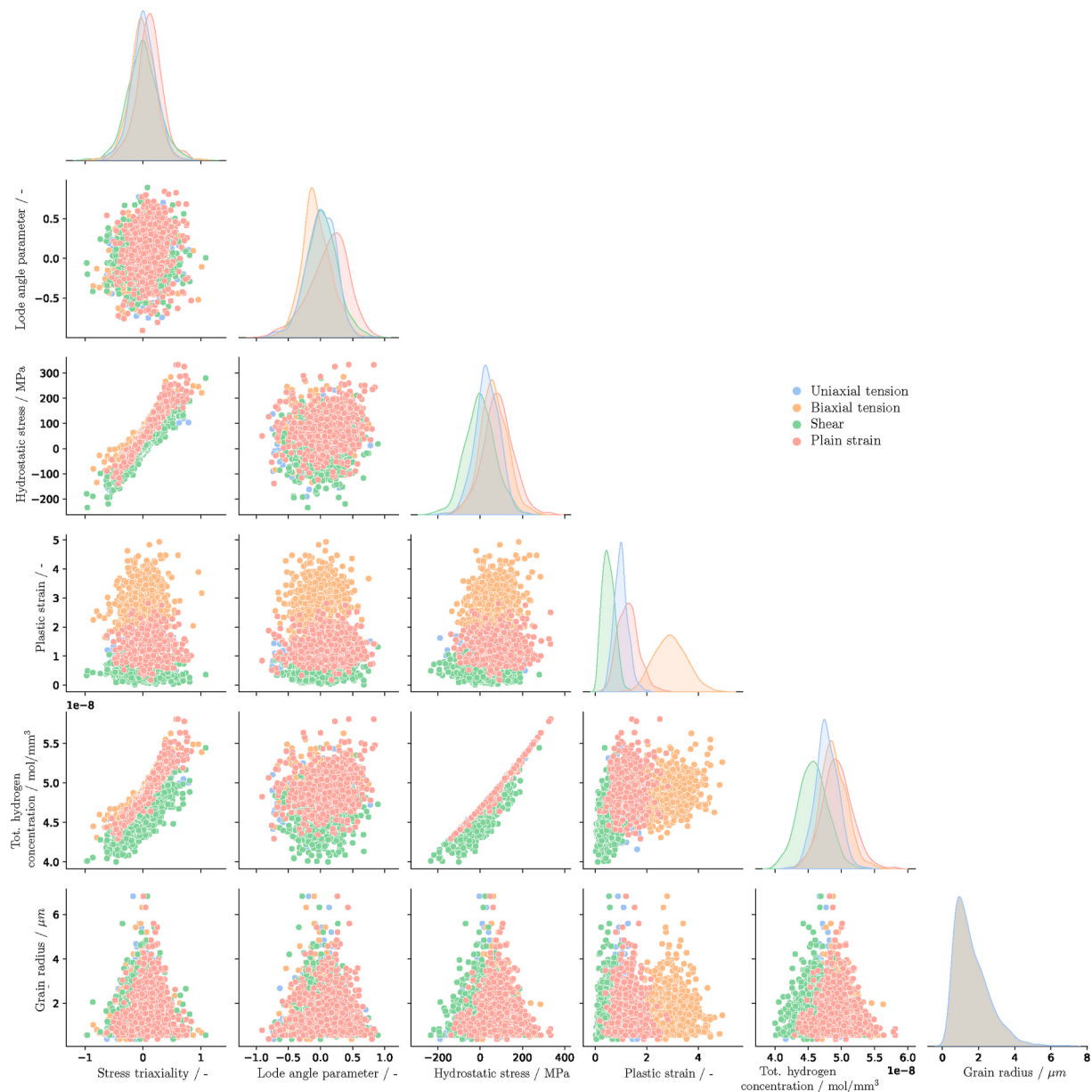


**Fig. 9.** Pairplot of averaged stress triaxiality, Lode angle parameter, hydrostatic stress, plastic strain and total hydrogen concentration per grain radius in RVEs without non-metallic inclusions.

the work reported in this paper.

#### Acknowledgments

The authors would like to thank Central Facility of Electron Microscopy (GFE) in RWTH Aachen for performing the EBSD measurements. Simulations were performed with computing resources granted by RWTH Aachen University under project <rwth1217>.

#### References

- [1] Veziroglu TN. 21st century's energy: hydrogen energy system. In: Sheffield JW, Sheffield C, editors. Assessment of hydrogen energy for sustainable development. Springer Netherlands; 2007. p. 9–31. ISBN 978-1-4020-6442-5.
- [2] Abe JO, Popoola API, Ajenifuja E, Popoola OM. Hydrogen energy, economy and storage: review and recommendation. Int J Hydrogen Energy 2019;44(29):15072–86. <https://doi.org/10.1016/j.ijhydene.2019.04.068>. URL: <https://www.sciencedirect.com/science/article/pii/S036031991931465X>.
- [3] Commission, E.. The european green deal. Communication from the Commission to the European Parliament, the European Council, the Council, the European Economic and Social Committee and the Committee of the Regions, COM; 2019. p. 640.
- [4] Commission, E.. RepowerEU. A plan to rapidly reduce dependence on Russian fossil fuels and fast forward the green transition. Off J Eur Union; 2022.
- [5] Lambert LA, Tayah J, Lee-Schmid C, Abdalla M, Abdallah I, Ali AHM, et al. The eu's natural gas cold war and diversification challenges. Energy Strategy Rev 2022; 43:100934. <https://doi.org/10.1016/j.esr.2022.100934>, URL: <https://www.sciencedirect.com/science/article/pii/S2211467X22001286>.
- [6] Commission, E.. Opinion of the european economic and social committee on communication from the commission to the european parliament, the council, the european economic and social committee and the committee of the regions: 'fit for 55': delivering the eu's 2030 climate target on the way to climate neutrality [com (2021) 550 final]. Off J Eur Union; 2021.
- [7] Wang A, van der Leun K, Peters D, Buseman M. European Hydrogen Backbone, how a dedicated hydrogen infrastructure can be created. 2020.
- [8] Jens J, Wang A, van der Leun K, Peters D, Buseman M. Extending the European Hydrogen Backbone, a european hydrogen infrastructure vision covering 21 countries. 2021.
- [9] Findley KO, O'Brien MK, Nako H. Critical assessment 17: mechanisms of hydrogen induced cracking in pipeline steels. Mater Sci Technol 2015;31(14):1673–80. <https://doi.org/10.1080/02670836.2015.1121017>.
- [10] Mohitadi-Bonab MA, Szpunar JA, Basu R, Eskandari M. The mechanism of failure by hydrogen induced cracking in an acidic environment for api 5l x70 pipeline

- steel. Int J Hydrogen Energy 2015;40(2):1096–107. URL: <https://www.sciencedirect.com/science/article/pii/S036031991403136X>.
- [11] Dunne DP, Hejazi D, Saleh AA, Haq AJ, Calka A, Pereloma EV. Investigation of the effect of electrolytic hydrogen charging of x70 steel: I. the effect of microstructure on hydrogen-induced cold cracking and blistering. Int J Hydrogen Energy 2016;41(28):12411–23. URL: <https://www.sciencedirect.com/science/article/pii/S0360319915314476>.
- [12] Ghosh G, Rostron P, Garg R, Panday A. Hydrogen induced cracking of pipeline and pressure vessel steels: a review. Eng Fract Mech 2018;199:609–18. URL: <https://www.sciencedirect.com/science/article/pii/S0013794418301024>.
- [13] Hoschke J, Chowdhury MPW, Venezuela J, Atrens A. A review of hydrogen embrittlement in gas transmission pipeline steels. Corrosion Rev 2023;41(3):277–317. URL: <https://doi.org/10.1515/correv-2022-0052>.
- [14] D.C.W. National transportation safety board. 2003. Natural gas pipeline rupture and fire near Carlsbad, New Mexico, August 19, 2000. Pipeline Accident Report NTSB/PAR-03/01; 2003.
- [15] Griffith AA. The phenomena of rupture and flow in solids. Philos Trans R Soc Lond - Ser A Contain Pap a Math or Phys Character 1921;221:163–98. URL: <https://doi.org/10.1098/rsta.1921.0006>.
- [16] Zapfe C, Sims C. Hydrogen embrittlement, internal stress and defects in steel. Trans Aime 1941;145:225–71. 1941.
- [17] Traidia A, Alfano M, Lubineau G, Duval S, Sherik A. An effective finite element model for the prediction of hydrogen induced cracking in steel pipelines. Int J Hydrogen Energy 2012;37(21):16214–30. URL: <https://www.sciencedirect.com/science/article/pii/S0360319912018484>.
- [18] Martin ML, Sofronis P. Hydrogen-induced cracking and blistering in steels: a review. J Nat Gas Sci Eng 2022;101:104547. URL: <https://www.sciencedirect.com/science/article/pii/S1875510022001378>.
- [19] Falkenberg R, Brocks W, Dietzel W, Scheider I. Modelling the effect of hydrogen on ductile tearing resistance of steels. Dedicated to Professor Dr Hermann Riedel on the occasion of his 65th birthday 2010;101(8):989–96. URL: <https://doi.org/10.3139/146.110368>.
- [20] Beachem CD. A new model for hydrogen-assisted cracking (hydrogen “embrittlement”). Metall Trans A 1972;3(2):441–55. URL: <https://doi.org/10.1007/BF02642048>.
- [21] Birnbaum HK, Sofronis P. Hydrogen-enhanced localized plasticity—a mechanism for hydrogen-related fracture. Mater Sci Eng, A 1994;176(1):191–202. URL: <http://www.sciencedirect.com/science/article/pii/092150939490975X>.
- [22] Taha A, Sofronis P. A micromechanics approach to the study of hydrogen transport and embrittlement. Eng Fract Mech 2001;68(6):803–37. URL: <https://www.sciencedirect.com/science/article/pii/S0013794400001260>.
- [23] Scott TE, Troiano AR. Interstitials and fracture of metals. Nature 1960;185(4710):372–3. URL: <https://doi.org/10.1038/185372a0>.
- [24] Oriani RA, Josephic PH. Equilibrium aspects of hydrogen-induced cracking of steels. Acta Metall 1974;22(9):1065–74. URL: <https://www.sciencedirect.com/science/article/pii/0001616074900613>.
- [25] Olden V, Thaulow C, Johnsen R. Modelling of hydrogen diffusion and hydrogen induced cracking in supermartensitic and duplex stainless steels. Mater Des 2008;29(10):1934–48. URL: <https://www.sciencedirect.com/science/article/pii/S0261306908001076>.
- [26] Lynch S. Progress towards understanding mechanisms of hydrogen embrittlement and stress corrosion cracking. 2007; vol. All Days. NACE-07493. In: Corrosion; 2007.
- [27] Yazdipour N, Haq AJ, Muzaka K, Pereloma EV. 2d modelling of the effect of grain size on hydrogen diffusion in x70 steel. Comput Mater Sci 2012;56:49–57. URL: <https://www.sciencedirect.com/science/article/pii/S0927025612000213>.
- [28] Arenas-Salcedo JG, Godinez-Salcedo JG, Gonzalez-Velazquez JL, Medina-Huerta JM. Effect of carbon content and microstructure on the diffusion of hydrogen in low carbon steels. Int J Electrochem Sci 2020;15(11):11606–22. URL: <https://doi.org/10.20964/2020.11.39>. URL: <Go to ISI>;//WOS:000591930300075.
- [29] Hussein A, Krom AHM, Dey P, Sunnardianto GK, Moulton OA, Walters CL. The effect of hydrogen content and yield strength on the distribution of hydrogen in steel: a diffusion coupled micromechanical fem study. Acta Mater 2021;209:116799. URL: <https://www.sciencedirect.com/science/article/pii/S1359645421001798>.
- [30] Döhl M, Tekkaya B, Münnemann S. Numerical investigation of the influence of non-metallic inclusions on the local hydrogen concentration under consideration of residual stress fields. Steel Res Int 2023. URL: <https://doi.org/10.1002/srin.202300309>. n/a(n/a).
- [31] Ilin DN, Saintier N, Olive JM, Abgrall R, Aubert I. Simulation of hydrogen diffusion affected by stress-strain heterogeneity in polycrystalline stainless steel. Int J Hydrogen Energy 2014;39(5):2418–22. URL: <https://www.sciencedirect.com/science/article/pii/S0360319913027900>.
- [32] Tao P, Gong J, Wang Y, Cen W, Zhao J. Modeling of hydrogen diffusion in duplex stainless steel based on microstructure using finite element method. Int J Pres Ves Pip 2020;180:104031. URL: <https://www.sciencedirect.com/science/article/pii/S0308016118305118>.
- [33] Hassan Hu, Govind K, Hartmaier A. Micromechanical modelling of coupled crystal plasticity and hydrogen diffusion. Phil Mag 2019;99(1):92–115. URL: <https://doi.org/10.1080/14786435.2018.1530466>.
- [34] Kumar R, Meena D, Mahajan DK. Modelling of fatigue crack initiation in hydrogen charged polycrystalline nickel. Procedia Struct Integr 2019;14:668–75. URL: <https://www.sciencedirect.com/science/article/pii/S2452321619300897>.
- [35] Zhang J, Su J, Zhang B, Zong Y, Yang Z, Zhang C, et al. Phase-field modeling of hydrogen diffusion and trapping in steels. Acta Metall Sin 2021;34(10):1421–6. URL: <https://doi.org/10.1007/s40195-021-01241-1>.
- [36] Mohitadi-Bonab M, Mousavi H, Pourazizi R, Szpunar J. Finite element modeling of hlc propagation in pipeline steel with regard to experimental observations. Int J Hydrogen Energy 2020;45(43):23122–33. URL: <https://www.sciencedirect.com/science/article/pii/S0360319920321911>.
- [37] Vajragupta N, Wechselwananee P, Lian J, Sharaf M, Münnemann S, Ma A, et al. The modeling scheme to evaluate the influence of microstructure features on microcrack formation of dp-steel: the artificial microstructure model and its application to predict the strain hardening behavior. Comput Mater Sci 2014;94:198–213. URL: <https://www.sciencedirect.com/science/article/pii/S0927020514002432>.
- [38] Roters F, Eisenlohr P, Hanterl C, Tjahjanto DD, Bieler TR, Raabe D. Overview of constitutive laws, kinematics, homogenization and multiscale methods in crystal plasticity finite-element modeling: theory, experiments, applications. Acta Mater 2010;58(4):1152–211. URL: <https://www.sciencedirect.com/science/article/pii/S1359645409007617>.
- [39] Krönen E. Zur plastischen Verformung des Vielkristalls. Acta Metall 1961;9(2):155–61. URL: <https://www.sciencedirect.com/science/article/pii/000161601900608>.
- [40] Rice JR. Inelastic constitutive relations for solids: an internal-variable theory and its application to metal plasticity. J Mech Phys Solid 1971;19(6):433–55. URL: <http://www.sciencedirect.com/science/article/pii/002250967190010X>.
- [41] Hutchinson JW. Bounds and self-consistent estimates for creep of polycrystalline materials. Proceedings of the Royal Society of London Series A 1976;348(1652):101–27. URL: <https://doi.org/10.1098/rspa.1976.0027>.
- [42] Pierce D, Asaro RJ, Needleman A. An analysis of non-uniform and localized deformation in ductile single crystals. Acta Metall 1983;31.
- [43] Vitek V, Mrovec M, Bassani J. Influence of non-glide stresses on plastic flow: from atomistic to continuum modeling. Mater Sci Eng, A 2004;365:31–7. URL: <https://doi.org/10.1016/j.msea.2003.09.004>.
- [44] Vajragupta N. The artificial microstructure model and its applications on plasticity and damage of the dual phase steel. Thesis; 2015. <https://publications.rwth-aachen.de/record/538976;zsfassung.in.dt.und.engl.Sprache.Zugl.:Aachen,Techn.Hochsch.Diss.,2015>.
- [45] Frederick CO, Armstrong P. A mathematical representation of the multiaxial bauscinger effect. Mater A T High Temp 2007;24:1–26. URL: <https://doi.org/10.3184/096034007X207589>.
- [46] Oriani R. The diffusion and trapping of hydrogen in steel. Acta Metall 1970;18(1):147–57. URL: <https://www.sciencedirect.com/science/article/pii/0001616079000787>.
- [47] Sofronis P, McMeeking RM. Numerical analysis of hydrogen transport near a blunting crack tip. J Mech Phys Solid 1989;37(3):317–50. URL: <https://www.sciencedirect.com/science/article/pii/0022509689900021>.
- [48] Barrera O, Tarleton E, Tang HW, Cocks ACF. Modelling the coupling between hydrogen diffusion and the mechanical behaviour of metals. Comput Mater Sci 2016;122:219–28. URL: <http://www.sciencedirect.com/science/article/pii/S0927025616302658>.
- [49] Kummick AJ, Johnson HH. Deep trapping states for hydrogen in deformed iron. Acta Metall; (United States) 1980;28:1. URL: <https://www.osti.gov/biblio/5242811>.
- [50] Dadfarinia M, Sofronis P, Neeraj T. Hydrogen interaction with multiple traps: can it be used to mitigate embrittlement? Int J Hydrogen Energy 2011;36(16):10141–8. URL: <https://www.sciencedirect.com/science/article/pii/S0360319911011815>.
- [51] Peng Z, Liu J, Huang F, Hu Q, Cao C, Hou S. Comparative study of non-metallic inclusions on the critical size for hlc initiation and its influence on hydrogen trapping. Int J Hydrogen Energy 2020;45(22):12616–28. URL: <https://www.sciencedirect.com/science/article/pii/S0360319920307126>.
- [52] Henrich M, Pütz F, Münnemann S. A novel approach to discrete representative volume element automation and generation-dragen. Materials 2020;13(8). URL: [https://mdpi-res.com/d\\_attachment/materials/materials-13-01887/article\\_deploy/materials-13-01887.pdf](https://mdpi-res.com/d_attachment/materials/materials-13-01887/article_deploy/materials-13-01887.pdf).
- [53] Pütz F, Henrich M, Fehlemann N, Roth A, Münnemann S. Generating input data for microstructure modelling: a deep learning approach using generative adversarial networks. Materials 2020;13(19):4236. URL: <https://doi.org/10.3390/ma13194236>.
- [54] Fehlemann N, Sparrer Y, Pütz F, Konemann M, Münnemann S. Influence of synthetically generated inclusions on the stress accumulation and concentration in x65 pipeline steel. IOP Conf Ser Mater Sci Eng 2021;1157(1):12056. URL: <https://doi.org/10.1088/1757-899X/1157/1/012056>.
- [55] Henrich M, Fehlemann N, Bexten F, Neite M, Kong L, Shen F, et al. Dragen - a deep learning supported rve generator framework for complex microstructure models. Heliyon 2023;19003URL: <https://www.sciencedirect.com/science/article/pii/S2405844023062114>.
- [56] Bachmann F, Hieltscher R, Schaeben H. Grain detection from 2d and 3d ebsd data—specification of the mtex algorithm. Ultramicroscopy 2011;111(12):1720–33. URL: <https://www.sciencedirect.com/science/article/pii/S0304399111001951>.
- [57] Tarjus G, Schauf P, Talbot J. Random sequential addition: a distribution function approach. J Stat Phys 1991;63(1):167–202. URL: <https://doi.org/10.1007/BF01026598>.
- [58] Torquato S. Optimal design of heterogeneous materials. Annu Rev Mater Res 2010;40(1):101–29. URL: <https://www.annualreviews.org/doi/abs/10.1146/annurev-matsci-070909-104517>.

- [59] Mulchrone KF, Choudhury KR. Fitting an ellipse to an arbitrary shape: implications for strain analysis. *J Struct Geol* 2004;26(1):143–53. URL: <https://www.sciencedirect.com/science/article/pii/S0191814103000932>.
- [60] Smit RJM, Brekelmans WAM, Meijer HEH. Prediction of the mechanical behavior of nonlinear heterogeneous systems by multi-level finite element modeling. *Comput Methods Appl Mech Eng* 1998;155(1):181–92. URL: <https://www.sciencedirect.com/science/article/pii/S0045782597001394>.
- [61] Wu W, Owino J, Al-Ostaz A, Cai L. Applying periodic boundary conditions in finite element analysis. 2014.
- [62] Huang F, Liu J, Deng ZJ, Cheng JH, Lu ZH, Li XG. Effect of microstructure and inclusions on hydrogen induced cracking susceptibility and hydrogen trapping efficiency of x120 pipeline steel. *Mater Sci Eng, A* 2010;527(26):6997–7001. URL: <https://www.sciencedirect.com/science/article/pii/S0921509310007604>.
- [63] Jin TY, Liu ZY, Cheng YF. Effect of non-metallic inclusions on hydrogen-induced cracking of api5l x100 steel. *Int J Hydrogen Energy* 2010;35(15):8014–21. URL: <https://www.sciencedirect.com/science/article/pii/S0360319910010591>.
- [64] Du XS, Cao WB, Wang CD, Li SJ, Zhao JY, Sun YF. Effect of microstructures and inclusions on hydrogen-induced cracking and blistering of a537 steel. *Mater Sci Eng, A* 2015;642:181–6. URL: <https://www.sciencedirect.com/science/article/pii/S0921509315301386>.
- [65] Samarasikera I. Hot rolling. ISBN 978-0-08-043152-9. In: Buschow KJ, Cahn RW, Flemings MC, Ilschner B, Kramer EJ, Mahajan S, et al., editors. Encyclopedia of materials: science and technology. Oxford: Elsevier; 2001. p. 3836–43. URL: <https://www.sciencedirect.com/science/article/pii/B0080431526006835>.
- [66] Haq AJ, Muzaka K, Dunne DP, Calka A, Pereloma EV. Effect of microstructure and composition on hydrogen permeation in x70 pipeline steels. *Int J Hydrogen Energy* 2013;38(5):2544–56. URL: <https://www.sciencedirect.com/science/article/pii/S036031991202616X>.
- [67] Dong CF, Liu ZY, Li XG, Cheng YF. Effects of hydrogen-charging on the susceptibility of x100 pipeline steel to hydrogen-induced cracking. *Int J Hydrogen Energy* 2009;34(24):9879–84. URL: <https://www.sciencedirect.com/science/article/pii/S0360319909015304>.
- [68] Liu ZY, Wang XZ, Du CW, Li JK, Li XG. Effect of hydrogen-induced plasticity on the stress corrosion cracking of x70 pipeline steel in simulated soil environments. *Mater Sci Eng, A* 2016;658:348–54. URL: <https://www.sciencedirect.com/science/article/pii/S0921509316301356>.
- [69] Peng Z, Liu J, Huang F, Hu Q, Cheng Z, Liu S, et al. Effect of submicron-scale mns inclusions on hydrogen trapping and hic susceptibility of x70 pipeline steels. *Steel Res Int* 2018;89(7):1700566. URL: <https://onlinelibrary.wiley.com/doi/abs/10.1002/srin.201700566>.
- [70] Peng Z, Liu J, Huang F, Zhang S, Hu Q, Wang Z, et al. The significance of inclusion morphology and composition in governing hydrogen transportation and trapping in steels. *Int J Hydrogen Energy* 2021;46(56):28811–22. URL: <https://www.sciencedirect.com/science/article/pii/S0360319921022473>.
- [71] Hirth JP. Effects of hydrogen on the properties of iron and steel. *Metall Trans A* 1980;11(6):861–90. <https://doi.org/10.1007/BF02654700>.
- [72] Li D, Gangloff RP, Scully JR. Hydrogen trap states in ultrahigh-strength aermet 100 steel. *Metall Mater Trans* 2004;35(3):849–64. <https://doi.org/10.1007/s11661-004-0011-1>.
- [73] Koyama M, Tasan CC, Akiyama E, Tsuzaki K, Raabe D. Hydrogen-assisted decohesion and localized plasticity in dual-phase steel. *Acta Mater* 2014;70:174–87. URL: <https://www.sciencedirect.com/science/article/pii/S135964541400069X>.
- [74] Wang S, Martin ML, Robertson IM, Sofronis P. Effect of hydrogen environment on the separation of fe grain boundaries. *Acta Mater* 2016;107:279–88. URL: <https://www.sciencedirect.com/science/article/pii/S1359645416300647>.
- [75] Trautmann A, Mori G, Oberndorfer M, Bauer S, Holzer C, Dittmann C. Hydrogen uptake and embrittlement of carbon steels in various environments. *Materials* 2020;13(16):3604. <https://doi.org/10.3390/ma13163604>.